molecules

MDPI

Article

Planar Elongated B_{12} Structure in M_3B_{12} Clusters (M = Cu-Au)

José Solar-Encinas [1], Alejandro Vásquez-Espinal [2,*], Luis Leyva-Parra [1], Osvaldo Yañez [3], Diego Inostroza [1], Maria Luisa Valenzuela [4], Walter Orellana [5] and William Tiznado [6,*]

[1] Programa de Doctorado en Fisicoquímica Molecular, Facultad de Ciencias Exactas, Universidad Andrés Bello, Av. República 275, Santiago 8370146, Chile
[2] Química y Farmacia, Facultad de Ciencias de la Salud, Universidad Arturo Prat, Casilla 121, Iquique 1100000, Chile
[3] Facultad de Ingeniería y Negocios, Universidad de las Américas, Santiago 7500000, Chile
[4] Grupo de Investigación en Energía y Procesos Sustentables, Instituto de Ciencias Químicas Aplicadas, Facultad de Ingeniería, Universidad Autónoma de Chile, Av. El Llano Subercaseaux 2801, Santiago 8900000, Chile
[5] Departamento de Ciencias Físicas, Universidad Andrés Bello, Santiago 8370136, Chile
[6] Computational and Theoretical Chemistry Group, Departamento de Ciencias Química, Facultad de Ciencias Exactas, Universidad Andrés Bello, Av. República 275, Santiago 8370146, Chile
* Correspondence: alvasquez@unap.cl (A.V.-E.); wtiznado@unab.cl (W.T.)

Abstract: Here, it is shown that the M_3B_{12} (M = Cu-Au) clusters' global minima consist of an elongated planar B_{12} fragment connected by an in-plane linear M_3 fragment. This result is striking since this B_{12} planar structure is not favored in the bare cluster, nor when one or two metals are added. The minimum energy structures were revealed by screening the potential energy surface using genetic algorithms and density functional theory calculations. Chemical bonding analysis shows that the strong electrostatic interactions with the metal compensate for the high energy spent in the M_3 and B_{12} fragment distortion. Furthermore, metals participate in the delocalized π-bonds, which infers an aromatic character to these species.

Keywords: boron clusters; group 11 metals; potential energy surface; DFT computations; chemical bonding; aromaticity

Citation: Solar-Encinas, J.; Vásquez-Espinal, A.; Leyva-Parra, L.; Yañez, O.; Inostroza, D.; Valenzuela, M.L.; Orellana, W.; Tiznado, W. Planar Elongated B_{12} Structure in M_3B_{12} Clusters (M = Cu-Au). *Molecules* **2023**, *28*, 236. https://doi.org/10.3390/molecules28010236

Academic Editors: Felipe Fantuzzi and Marco A. C. Nascimento

Received: 24 November 2022
Revised: 22 December 2022
Accepted: 25 December 2022
Published: 28 December 2022

1. Introduction

Boron's electronic deficiency allows it to assemble into diverse architectures to form systems with unusual electronic properties, making it promising for applications in diverse technologies. For instance, in super hard materials, semiconductors, nanomaterials, and compounds with potential biological applications [1–10].

However, this structural versatility makes it challenging to establish chemical bonding patterns that facilitate these systems' structural rationalization. In contrast to its carbon neighbor in the periodic table, there are very limited models for predicting the structures of boron-based molecular systems. Boron hydrides, for instance, are characterized using electron counting-based rules [11–18].

Structures of bare B_n clusters have been thoroughly analyzed in recent years. These studies show that small clusters prefer planar structures up to a maximum size depending on the charge of the system. Cationic, neutral, and anionic clusters prefer planar structures up to 15, 20, and 40 atoms, respectively [19–42]. This demonstrates the significant effect that even one electron has on the structural preference of boron clusters.

In recent years, it has been shown that adding alkali metals to the B_{12} structure induces fascinating structural changes. For instance, in the LiB_{12} global minimum (GM) structure, the naked cluster B_{12} structure remains almost unchanged [43], but LiB_{12}^- and NaB_{12}^- GMs prefer a conical shape with an inner B_4 ring and a higher concavity than the quasi-planar B_{12} cluster [44]. More noticeable is the D_{6d}-Li_2B_{12} GM, a tubular structure consisting of two

stacked B_6 rings capped with Li's along the main axis [43]. Interestingly, the other alkali metals (Na-Cs) do not induce relevant B_{12} structural changes, highlighting the Li role [44]. An additional Li, in Li_3B_{12}, favors a cage-like B_{12} structure [43]. The isomerization energy decomposition analysis (IEDA) [45] has proven to be an appropriate theoretical method that provides an insightful explanation for these structural preferences; an enhanced stabilizing electrostatic interaction between the Li cations and the 3D-B_{12} moiety counterbalances the energetic cost of distorting the B_{12} fragment. A systematic review of metal-doped boron clusters is reported elsewhere [46].

What about the group 11 elements (Cu, Ag, Au)? Since they form compounds with oxidation states of +1, they could transfer one electron to B_{12}, in analogy with the alkali metals. Our group has recently reported the minimum energy structures of CuB_{12} and CuB_{12}^-. In CuB_{12}, Cu is placed capping the B_9 ring of the B_{12}-nacked cluster. In the anion, there are significant structural changes, with Cu participating in the electronic delocalization responsible for the doubly aromatic character of this species [47]. In AuB_{12} and AuB_{12}, Au is bonded to one of the B's of the B_{12} peripheral ring without inducing significant changes in the B_{12} structure [48]. All these results are consistent with the vast structural opportunities feasible by doping boron clusters with different metals [49–56], demanding systematic studies of the structural preferences for different combinations. This becomes a challenge from computational chemistry as the number and kind of atoms conforming to the study system increase since it demands the help of algorithms that facilitate the potential energy surface (PES) exploration [57,58].

Here, we show that doping B_{12} with three Cu, Ag, or Au atoms favors an elongated planar structure not preferred in the B_{12} bare cluster. Our study involves the PES exploration, employing genetic algorithms in conjunction with density functional theory (DFT) calculations, of the M_nB_{12} combinations (M = Cu-Au, n = 1–3). Analysis of the chemical bonding and magnetic behavior shows that M_3B_{12} are local and global aromatic species. The structural analogs to the Li_nB_{12} global minima (n = 1–3) were also analyzed, showing that for n = 2 and 3, the structural preferences are drastically different. This highlights the importance of appropriate methods to provide reliable information on the energetically preferred structures of metal-doped boron clusters.

2. Results and Discussion

The putative GM structures of M_nB_{12} (M = Cu-Au and n = 1–3) clusters are depicted in Figure 1, and relevant lowest energy isomers are depicted in Figures S1–S9. Figure 1 shows that the B_{12} structure of the bare cluster is retained at the GM by adding one and two metal atoms. The first metal atom forms a bridged-like B-M-B bond with two boron atoms of the peripheral B_9 ring (**1**-M), while the second one is placed on one of the edges of the MB_2 triangle (**2**-M). Note that in previous reports the effect of doping B_{12} with other transition metals was evaluated, revealing that metal is placed on the main axis, above the peripheral B_9 ring on the concave side of the B_{12} structure [49–54], which in the present work has been identified as an isomer close in energy to the putative global minimum of CuB_{12} (structure 1b, Figure S1). In the case of AgB_{12} and AuB_{12}, this structure does not correspond to a local minimum since it has an imaginary frequency, and therefore is not reported. Furthermore, the analogous to the GM structures reported for the ZrB_{12} and AlB_{12} combinations [55,56] have relative energies higher than 20.0 kcal mol^{-1}, thus lying above the relative energy range considered in our report. For the M_nB_{12} (M = Cu-Au and n = 1–3) clusters, there are marginal changes in the B-B bond distances due to the addition of metals, more significant in the fragment where the metal is bonded. This agrees with the bond orders according to the $WBI_{B\text{-}B}$ values, which are in the range of 0.4–1.3 in both the B_{12} and the M_nB_{12} clusters (M = Cu-Au, n = 1, 2), where values close to or greater than 1.0 are among the peripheral atoms, as can be seen in Figure S10.

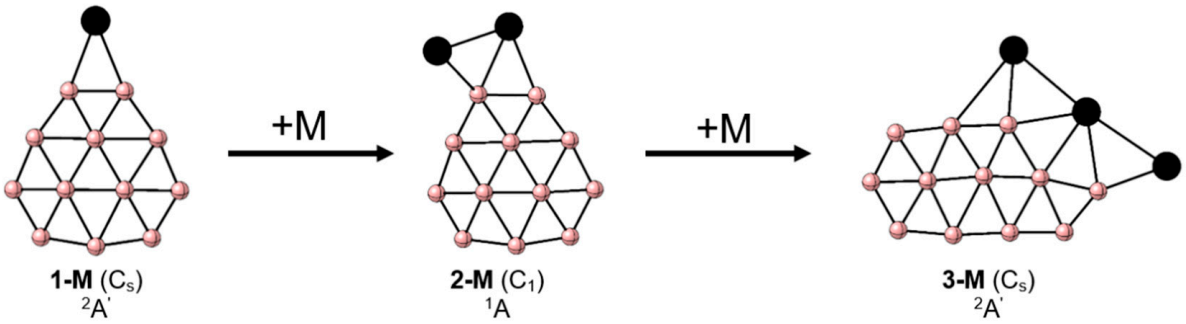

Figure 1. Lowest energy structures for M_nB_{12} clusters (M = Cu-Au and n = 1–3) at the PBE0-D3/def2-TZVP level. M: black spheres, B: pink spheres.

The WBI_{M-B} values are less than 1.0 for the bridged metal and close to 1.0 for the metal bonded to one boron at the periphery, while the WBI_{M-M} value in **2**-M is less than 0.1, showing that metals lack a significant covalent bonding character. When one more metal is added, in M_3B_{12}, the minimum energy structure has a significantly different B_{12} fragment than that of the B_{12} GM. An elongated planar structure is now favored, **3**-M (Figure 1). The stabilizing role of M to tend planar elongated structure is significant, as evidenced in Figure 2, which shows how the relative energy of this motif decreases as M atoms are added to become the GM in M_3B_{12}. WBI_{B-B} values range from 0.4 to 1.4, with values near or above 1.0 among the outer borons. One of the M atoms closes the elongated ring, while the other two are linked at the periphery in bridged positions with the M-B edges, the three metal atoms forming a linear M_3 structure. The WBI_{M-B} values between the extreme M and B are the highest, more significant than 0.5, while the WBI_{M-B} values involving the central M are lower (see Figures S11 and S12). The charges from the natural population analysis (NPA) indicate a charge transfer from the M to the B_{12} fragment (q_M = 0.2–0.7 |e|); however, it does not reach the magnitude of the alkali atoms, where almost one electron per metal atom is transferred (Figures S10–S12). Additionally, the natural electron configurations of the Cu, Ag, and Au atoms in these systems are reported in Table S1. The charge transfer occurs mainly from the 4s and 5s orbitals of Cu and Ag, respectively. While for systems with Au, this transfer, to a lesser extent, occurs from the 5d orbitals.

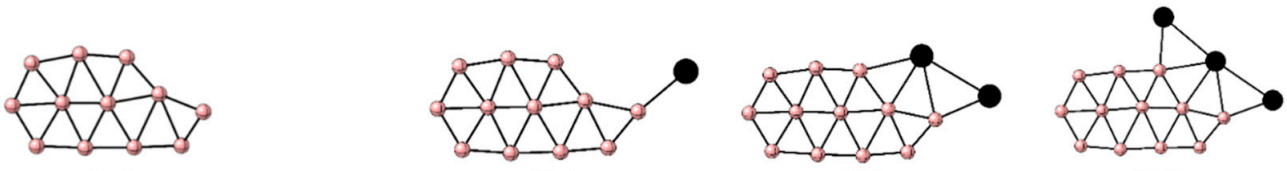

Figure 2. Stabilization of the elongated planar B_{12} fragment as it is doped with M atoms in M_nB_{12} clusters (M = Cu-Au and n = 1–3). Structures were optimized at the PBE0-D3/def2-TZVP level. The relative energies are also reported in kcal mol^{-1} (regarding GM for each combination). M: black spheres, B: pink spheres.

After reviewing the identified structures, we realized that the counterpart structures of the Li_nB_{12} (n = 2, 3) GMs were missing. This prompted us to evaluate these geometries, and as shown in Figure 3, the relative energies when Li is replaced by group 11 metals change significantly. This underlines the importance of using suitable algorithms to explore the PES since it is unreliable to use structural knowledge of related systems, which could lead to entirely wrong conclusions. The structural counterparts are local minima, except for Au_2B_{12}

and Au_3B_{12}, with two and one imaginary frequencies. Remarkably, for M = Ag and Au, the relative energies are at least 50.0 kcal mol^{-1} above the GM identified by PES exploration.

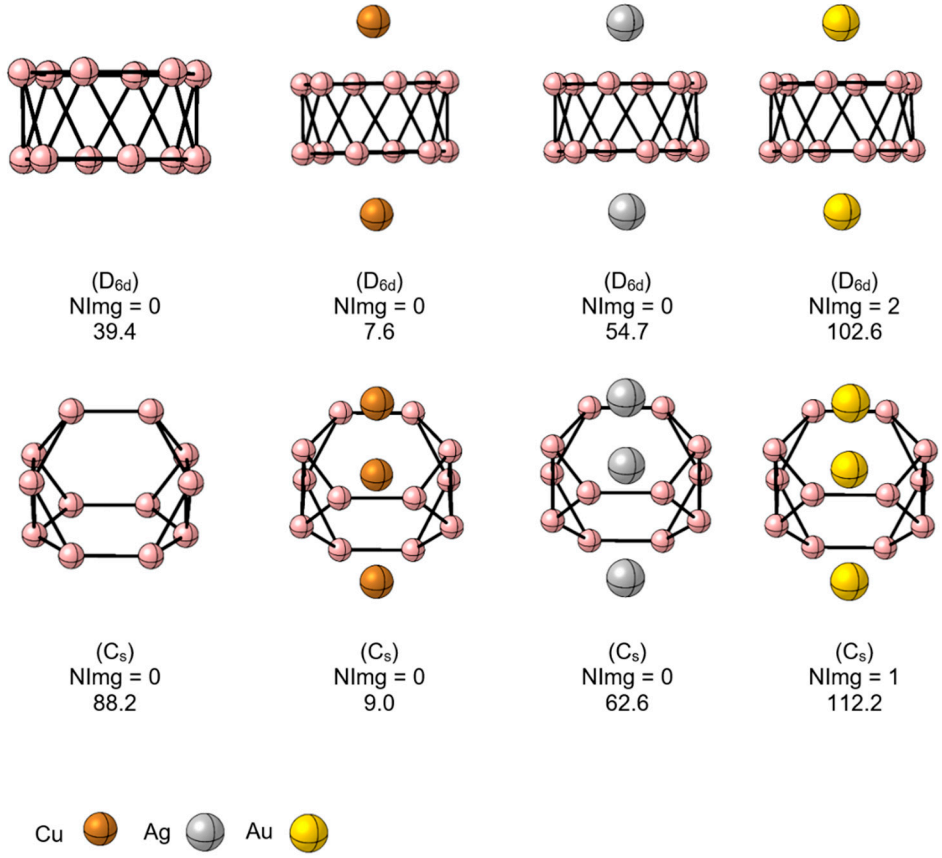

Figure 3. Optimized structures for M_nB_{12} (M = Cu-Au and n = 2, 3) in analogous geometries to the global minima of Li_2B_{12} and Li_3B_{12} clusters, and their relative energies (kcal mol^{-1}) concerning the corresponding GMs, at the PBE0-D3/def2-TZVP level.

To gain further insights into the chemical bonding, we performed an AdNDP analysis. Orbital localization methods proved insightful in understanding chemical bonding in boron clusters [59,60]. The results of the AdNDP analysis for all systems are reported in Figures S13–S15. In the three systems **1**-M, **2**-M, and **3**-M, five, ten, and fifteen 1c-2e lone pairs are identified, corresponding to the d orbitals of the metals of each system. For **1**-M and **2**-M, the bonding picture of the B_{12} fragment remains identical to that of the bare B_{12} cluster (see Figures S13 and S14). In **1**-M, the metal connects to the B_{12} fragment through a three-center one-electron (3c-1e) B-M-B σ-bond, as shown in Figure S13.

In the case of **2**-M, the bonding situation is very similar, only now the second M atom is attached to one of the periphery B's by one M-B 2c-2e σ-bond. Furthermore, the bridged M is now linked via a B-M-B 3c-2e σ-bond at the cost of delocalization of the periphery B-B bond. The **3**-M bonding will be discussed in more detail. For **3**-Cu, the localized orbitals, excluding the lone pairs, recovered by AdNDP are reported in Figure 4. The other systems show similar bonding patterns (see the full bonding picture in Figure S15). Eight B-B 2c-2e σ-bonds link the nine periphery borons. Seven 3c-2e σ-bonds are also detected between each triangular fragment that forms the three internal boron with those of the periphery. The M extremes of the M_3 fragment are linked to borons by M-B 2c-2e σ-bonds. The central M does not participate in any bonds, according to AdNDP. The remaining electrons, AdNDP locates in three π-orbitals, two of 6c-2e, and one of 4c-1e, for a total of five π-electrons. These results suggest the possibility of (anti)aromaticity, local or global, given both σ- and π-delocalized bonds. We will discuss below this possibility by analyzing the **3**-M magnetic behavior.

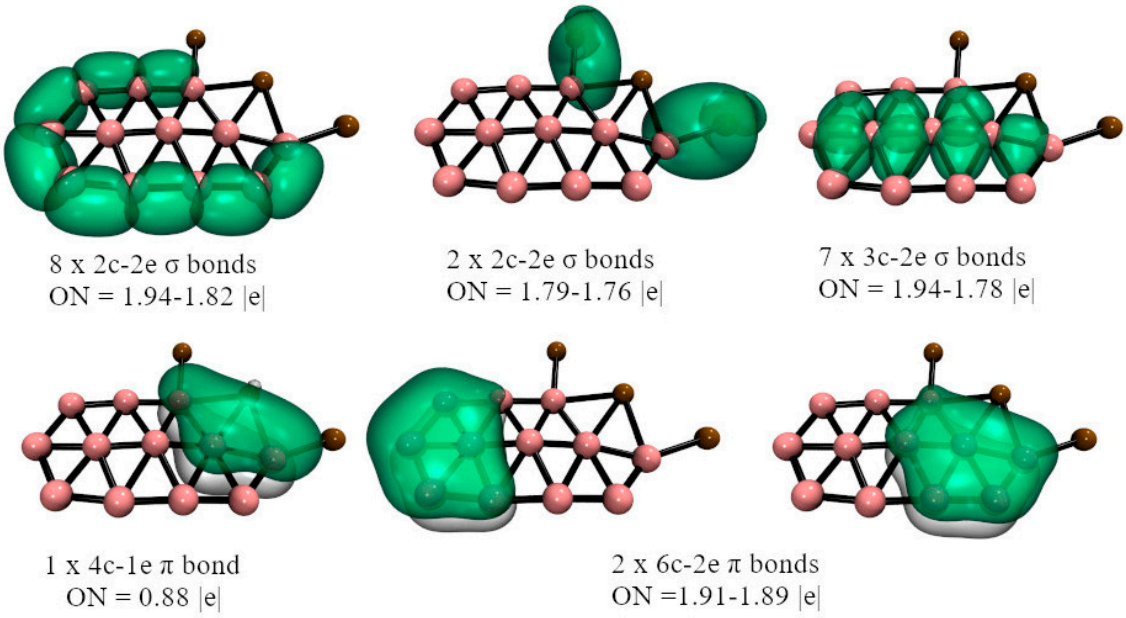

Figure 4. Chemical bonding representation according to the AdNDP method of **3**-Cu, at the PBE0-D3/Def2-TZVP level. Cu: brown spheres, B: pink spheres.

The shape of the **3**-M structure evokes the geometry of an isomer of its valence isoelectronic B_{13} cluster, which is 3.7 kcal mol^{-1} above the GM (at the PW91/TZ2P level) [61]. The AdNDP analysis of this system is shown in Figure 5, where it is seen that there are significant differences with **3**-M, the B_9 contour is closed by 10 B-B 2c-2e σ-bonds, there are six delocalized 4c-2e σ-bonds connecting the internal B_3 fragment to the B_9 contour, and AdNDP places seven electrons forming π-bonds. These bonding differences, i.e., having 4n delocalized σ-bonds, could be responsible for the non-planarity of B_{13}.

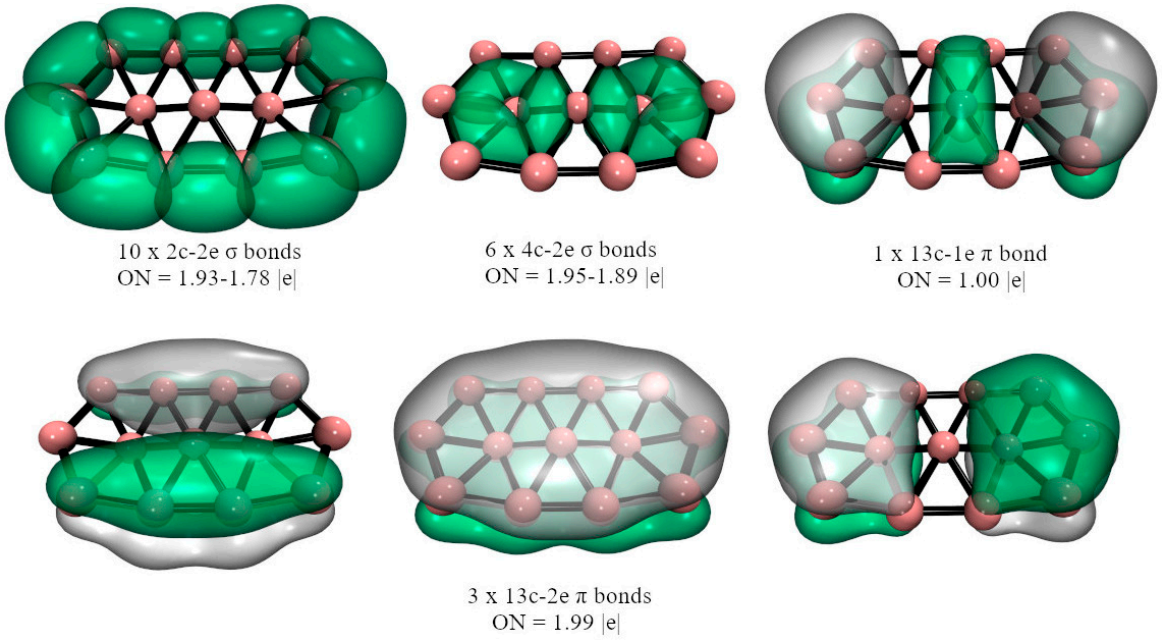

Figure 5. Chemical bonding representation according to the AdNDP method of B_{13}, at the PBE0-D3/Def2-TZVP level.

The isomerization energy decomposition analysis (IEDA) allows us to analyze quantitatively the structural preference between two isomers in terms of energy components [45].

A hypothetical thermodynamic cycle used to perform the IEDA in the M_3B_{12} systems is shown in Figure S16. Thus, we compare **3**-Cu vs. the first Cu_3B_{12} isomer that preserves the B_{12} fragment of the naked cluster (ΔE_{iso} = 13.0 kcal mol^{-1}); the relative energy is slightly different from that reported in Figure S7 since the IEDA calculations were performed at the PBE0-D3-BJ/ZORA/TZ2P level. The values summarized in Table 1 show that interactions favor GM in the orbital ($\Delta\Delta E_{orb}$ = 115.3 kcal mol^{-1}) contribution, compensating for the electrostatic ($\Delta\Delta V_{elstat}$ = –7.9 kcal mol^{-1}) and Pauli repulsion ($\Delta\Delta E_{Pauli}$ = –19.5 kcal mol^{-1}) terms which favor the higher energy isomer; the difference in the dispersion interaction is negligible. These results show that the covalent interactions between M_3 and the B_{12} are enhanced and are more important in terms of magnitude than ionic interactions in the GM, thus accounting for its preference. However, ΔE_{iso} also depends on the distortion energy of each fragment, favoring, in this case, the higher energy isomer ($\Delta\Delta E_{dist\ (total)}$ = –74.5 kcal mol^{-1}). Note that the major contribution of this term comes from the distortion of the M_3 fragment, while the B_{12} fragment slightly prefers the geometry it has in the GM. Therefore, Cu_3B_{12} prefers the planar elongated shape granted by better orbital interactions between the Cu_3 and B_{12} fragment, compensating for the energy cost to distort its M_3 moiety, and to a lesser extent, the unfavorable electrostatic interaction and Pauli repulsion terms. IEDA predicts a similar trend for Ag_3B_{12} with the difference that the Pauli repulsion term, in this case, also favors GM. Finally, for Au_3B_{12}, the results are slightly different. The distortion energies follow the same trends and magnitudes as for its lighter analogs, and the orbital interaction remains the most important term; however, the electrostatic interaction, which, as in Cu_3B_{12} and Ag_3B_{12}, favors the second isomer, is now comparable in magnitude to the orbital term, so that the balance of all the terms that make up ΔE_{iso} leaves both isomers virtually isoenergetic at the PBE0-D3-BJ/ZORA/TZ2P level. Note that although at the PBE0-D3/def2-TZVP level, the planar elongated system is still predicted to be the global minimum of Au_3B_{12}, the difference in energy between it and the highest energy isomer is much smaller (2.1 kcal mol^{-1}) than for Cu_3B_{12} and Ag_3B_{12}.

Table 1. IEDA results (kcal mol^{-1}) at the PBE0-D3-BJ/ZORA/TZ2P level for the M_3B_{12} clusters with M_3^{3+} + B_{12}^{3-} as fragments.

System	Cu_3B_{12}	Ag_3B_{12}	Au_3B_{12}
ΔE_{iso}	13.0	9.8	−0.2
ΔE_{dist} (M_3^{3+})	−82.1	−75.7	−73.2
ΔE_{dist} (B_{12}^{3-})	7.6	6.7	8.2
$\Delta\Delta E_{int}$	87.5	78.9	64.8
$\Delta\Delta E_{orb}$	115.3	85.2	86.8
$\Delta\Delta V_{elstat}$	−7.9	−22.5	−70.6
$\Delta\Delta E_{Pauli}$	−19.9	16.4	49.0
$\Delta\Delta E_{disp}$	0.0	−0.2	−0.4

AdNDP analysis reveals the presence of delocalized π-bonds, which could be associated with a possible (anti)aromatic character. To investigate this possibility, we have evaluated the current densities induced by an external magnetic field (perpendicular to the molecular plane). According to the magnetic criteria, an (anti)aromatic system is characterized by the presence of (diatropic) paratropic ring currents circuits. Figure 6 shows that **3**-Cu exhibits both local and global diatropic ring currents circuits. The local circuits are internal and around the inner B atoms. At the same time, the global ring current surrounds the cluster decorating the external M_3B_9 chain. By analyzing the integrated current profiles (Figures S17–S19), it has been possible to estimate the ring current strength (RCS) of each circuit (see Figure 6). RCS values are significant, considering benzene has a net RCS of 11.8 nA T^{-1} at the same level. The magnetic behavior of **3**-Ag and **3**-Au are similar, as shown in Figures S17–S19. Therefore, the **3**-M are classified as local and global aromatic species according to the magnetic criterion.

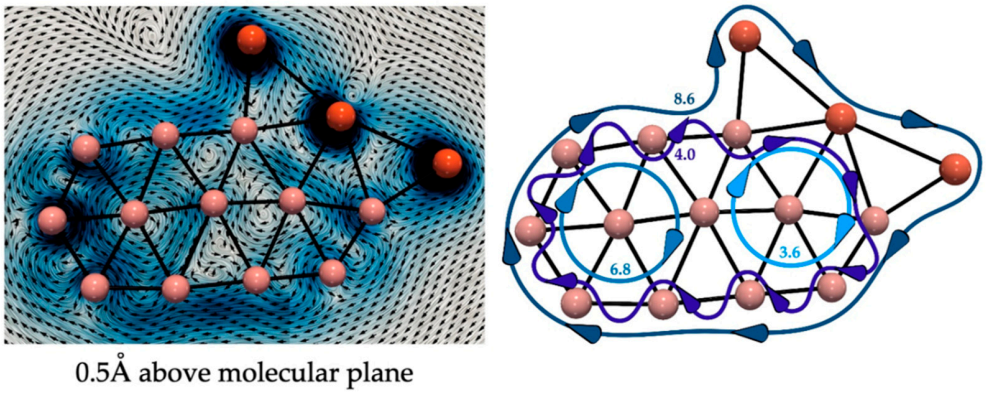

Figure 6. On the left, the magnetically induced current density of Cu_3B_{12} in a plane placed 0.5 A above the molecular plane. Diatropic currents are assumed to circle clockwise, and paratropic ones circle anticlockwise. On the right are the detected currents' paths and their strength (in nA T^{-1}).

3. Materials and Methods

We systematically explored the potential energy surfaces employing the AUTOMATON program [57,62], with an initial screening (in the singlet states) at the PBE0 [63]/SDDALL [64] level. The low-lying energy isomers (<20.0 kcal mol^{-1} above the putative global minimum) were re-minimized at the PBE0-D3 [65]/def2-TZVP [66] level. The top isomers were optimized in the triplet state at the PBE0-D3/def2-TZVP level to test the relative energies at this multiplicity. To provide more reliability in our energetic analysis, relative energies were computed using the domain-based local pair-natural orbital-based single-, double-, and perturbative triple excitations coupled cluster DLPNO-CCSD(T) method [67] as implemented in ORCA-4.2.1 [68,69] in conjunction with extrapolation to the complete basis set limit via the def2-SVP and def2-TZVP basis sets [70,71] (labeled as DLPNO-CCSD(T)/CBS). This refinement was performed for isomers up to 10.0 kcal mol^{-1} above the putative global minimum. The chemical bonding was analyzed (at the PBE0-D3/def2-TZVP level) using the Wiberg bond index (WBI) and natural population analysis (NPA), as implemented in the NBO 6.0 program [72]. Furthermore, the adaptive natural density partitioning (AdNDP) method [73,74] was performed with the Multiwfn program [75]. AdNDP represents the electronic structure in n-center-two-electron (nc-2e) bonds, with n ranging from one to the total number of atoms in the molecule, recovering the Lewis' electron pair concept as the fundamental chemical bonding component complemented with delocalized bonds, when they are present. Isomerization energy decomposition analysis (IEDA) [45] was computed. IEDA allows the decomposition of the isomerization energy (ΔE_{iso}) in terms of the distortion energy of the fragments (ΔE_{dist}) and the change in the interaction energies between the fragments of each isomer ($\Delta\Delta E_{int}$). The latter term, in turn, is decomposed as the sum of the changes in the orbital ($\Delta\Delta E_{orb}$) and electrostatic ($\Delta\Delta V_{elstat}$) interaction, the Pauli repulsion ($\Delta\Delta E_{Pauli}$), and the dispersion energy ($\Delta\Delta E_{disp}$). This analysis was performed at the PBE0-D3-BJ [76]/ZORA [77]/TZ2P [78] level using ADF2012 [79].

To assess aromaticity, we have analyzed the current densities induced by an external magnetic field applied perpendicularly to the molecular plane (at the PBE0-D3/def2-TZVP level) using the GIMIC program [80,81], which employs the gauge-included atomic orbitals (GIAO) method [82]. For vector plots, we used the Paraview 5.10.0 software [83,84]. The ring current strengths (RCS), a quantitative descriptor of aromaticity, were obtained by integrating the ring current flow in a perpendicular plane using the two-dimensional Gauss–Lobatto algorithm [80,85] as implemented in GIMIC. The integration planes correspond to cut-off planes perpendicular to the chosen bonds of the interest annular moiety and extend horizontally for 3.6 Å along the ring's plane, with 2.6 Å above and below the bond. Positive (diatropic), negative (paratropic), and near-zero RCS values indicate aromaticity, antiaromaticity, and non-aromaticity. The bisected current densities (sigma and

pi) were calculated using AIMAll software [86] at the PBE0-D3/def2-TZVP level. As previously established in other studies, the different ring current circuits have been identified by analyzing the RCS profiles in appropriate planes [87,88].

4. Conclusions

The effect of doping the B_{12} cluster with group 11 metals, in M_3B_{12} (M = Cu-Au) clusters is evaluated to compare with the impact of alkali metals, especially Li, where the minimum energy structures of Li_2B_{12} and Li_3B_{12} consist of B_{12} arrays quite different from those of the bare B_{12} cluster. Exploration of the potential energy surface, using genetic algorithms and DFT calculations, reveals that adding one or two metal atoms induces substantial changes in the B_{12} fragment, with minor modifications in bond distances, especially of the fragments in contact with the metals. However, when the third M atom is added, in M_3B_{12}, a structure containing a planar elongated B_{12} fragment (**3**-M), whose shape is high-energy in the bare cluster, is favored. This is evidence of the wealth of structural possibilities by doping boron clusters with metals, where the nature of the metal may have unexpected effects. The latter also evidences the need for adequate methods to identify minimum energy structures since no structural preferences can be assumed based on similar systems. For example, the GM analogous structures of Li_2B_{12} are less stable by at least 7 kcal mol^{-1}, while the Li_3B_{12} analogs are not even all local minima and are more than 50 kcal mol^{-1} away from the most stable one. Bonding analysis evidences the presence of delocalized σ- and π-bonds in **3**-M. Furthermore, magnetically induced current density analysis evidences the existence of local and global diatropic ring currents, characterizing them as aromatic.

Supplementary Materials: The following supporting information can be downloaded at: https://www.mdpi.com/article/10.3390/molecules28010236/s1, Figures S1–S9: Global minimum and low-lying isomers of M_nB_{12} (M = Cu-Au; n = 1–3), their point group symmetries and spectroscopic states. Relative energies are shown in kcal·mol^{-1} at PBE0-D3/def2-TZVP (in bold) level including zero-point energy (ZPE) corrections and DLPNO-CCSD(T)/CBS (red parenthesis). A number-letter label identifies structure to facilitate their connection with their Cartesian coordinates (at the end of the ESI); Figures S10–S12: Bond lengths (r, Å), natural charges (q, |e|), and Wiberg bond indices (WBI) of the M_nB_{12} (M = Cu-Au; n = 1–3) GMs at the PBE0-D3/def2-TZVP level; Figures S13–S15: The AdNDP bonding pattern of the M_nB_{12} (M = Cu-Au; n = 1–3) GMs at the PBE0-D3/def2-TZVP level; Figure S16: Energy cycle for the isomerization between the GM (top) and the higher energy isomer (bottom) of M_3B_{12} (M = Cu, Ag, Au) used in IEDA computations; Figures S17–S19: The susceptibility of density current for M_3B_{12} (M = Cu-Au) in a plane 0.5 Å above the molecular plane (vector plot). The scheme for identifying different ring current circuits through a computed profile of the ring current strength (RCS) passing selected planes. The RCS profiles and the identified ring current circuits with their respective RCS value in nA.T^{-1}; Table S1: Computed natural electron configurations of the Cu, Ag and Au atoms in the putative global minima of MB_{12}, M_2B_{12} and M_3B_{12} systems; Cartesian Coordinates of isomers of the M_nB_{12} (M = Cu, Ag, Au) (n = 1–3) clusters at the PBE0-D3/def2-TZVP level.

Author Contributions: Conceptualization, W.T., J.S.-E. and W.O.; methodology, J.S.-E., L.L.-P., A.V.-E., W.O., M.L.V. and O.Y.; software, D.I., O.Y. and W.O.; validation, W.T., J.S.-E., M.L.V., W.O. and A.V.-E.; formal analysis, W.T. and A.V.-E.; investigation, W.T., W.O. and O.Y.; resources, W.T. and M.L.V.; data curation, J.S.-E., L.L.-P., D.I. and O.Y.; writing—original draft preparation, W.T., J.S.-E. and A.V.-E.; writing—review and editing, all authors; visualization, J.S.-E., D.I. and O.Y.; supervision, W.T. and W.O.; project administration, W.T.; funding acquisition, W.T. and M.L.V. All authors have read and agreed to the published version of the manuscript.

Funding: This research was funded by FONDECYT grants number 1211128 and 1221019.

Institutional Review Board Statement: Not applicable.

Informed Consent Statement: Not applicable.

Data Availability Statement: Not applicable.

Acknowledgments: We thank the financial support of the National Agency for Research and Development (ANID) through FONDECYT projects 1211128 (W.T.) 1221019 (A. V-E.). National Agency for Research and Development (ANID)/Scholarship Program/BECAS DOCTORADO NACIONAL/2019-21190427 (D.I.). National Agency for Research and Development (ANID)/Scholarship Program/BECAS DOCTORADO NACIONAL/2020-21201177 (L.L-P.). Scholarship Program/BECAS DOCTORADO UNAB (J.S.-E). Powered@NLHPC: This research was partially supported by the supercomputing infrastructure of the NLHPC (ECM-02).

Conflicts of Interest: The authors declare no conflict of interest.

Sample Availability: Not applicable.

References

1. Akopov, G.; Yeung, M.T.; Kaner, R.B. Rediscovering the Crystal Chemistry of Borides. *Adv. Mater.* **2017**, *29*, 1604506. [CrossRef] [PubMed]
2. Scheifers, J.P.; Zhang, Y.; Fokwa, B.P.T. Boron: Enabling Exciting Metal-Rich Structures and Magnetic Properties. *Acc. Chem. Res.* **2017**, *50*, 2317–2325. [CrossRef] [PubMed]
3. An, Q.; Goddard, W.A. Improved Ductility of B_{12} Icosahedra-Based Superhard Materials through Icosahedral Slip. *J. Phys. Chem. C* **2017**, *121*, 11831–11838. [CrossRef]
4. Robinson, P.J.; Liu, G.; Ciborowski, S.; Martinez-Martinez, C.; Chamorro, J.R.; Zhang, X.; McQueen, T.M.; Bowen, K.H.; Alexandrova, A.N. Mystery of Three Borides: Differential Metal-Boron Bonding Governing Superhard Structures. *Chem. Mater.* **2017**, *29*, 9892–9896. [CrossRef]
5. Chen, W.; Li, Y.; Yu, G.; Li, C.Z.; Zhang, S.B.; Zhou, Z.; Chen, Z. Hydrogenation: A Simple Approach to Realize Semiconductor-Half-Metal-Metal Transition in Boron Nitride Nanoribbons. *J. Am. Chem. Soc.* **2010**, *132*, 1699–1705. [CrossRef]
6. Dai, X.; Zhang, L.; Li, J.; Li, H. Metal-Semiconductor Transition of Single-Wall Armchair Boron Nanotubes Induced by Atomic Depression. *J. Phys. Chem. C* **2017**, *121*, 26096–26101. [CrossRef]
7. Bud'ko, S.L.; Lapertot, G.; Petrovic, C.; Cunningham, C.E.; Anderson, N.; Canfield, P.C. Boron Isotope Effect in Superconducting MgB_2. *Phys. Rev. Lett.* **2001**, *86*, 1877–1880. [CrossRef]
8. Kazakov, S.M.; Puzniak, R.; Rogacki, K.; Mironov, A.V.; Zhigadlo, N.D.; Jun, J.; Soltmann, C.; Batlogg, B.; Karpinski, J. Carbon Substitution in MgB_2 Single Crystals: Structural and Superconducting Properties. *Phys. Rev. B Condens. Matter. Mater. Phys.* **2005**, *71*, 024533. [CrossRef]
9. Nakamura, H. Development of High Boron Content Liposomes and Their Promising Antitumor Effect for Neutron Capture Therapy. *Yakugaku Zasshi* **2013**, *133*, 1297–1306. [CrossRef]
10. Leśnikowski, Z.J. Challenges and Opportunities for the Application of Boron Clusters in Drug Design. *J. Med. Chem.* **2016**, *59*, 7738–7758. [CrossRef]
11. Ohishi, Y.; Kimura, K.; Yamaguchi, M.; Uchida, N.; Kanayama, T. Formation of Hydrogenated Boron Clusters in an External Quadrupole Static Attraction Ion Trap. *J. Chem. Phys.* **2008**, *128*, 124304. [CrossRef] [PubMed]
12. Szwacki, N.G.; Weber, V.; Tymczak, C.J. Aromatic Borozene. *Nanoscale Res. Lett.* **2009**, *4*, 1085–1089. [CrossRef] [PubMed]
13. Sahu, S.; Shukla, A. Probing Aromaticity of Borozene through Optical and Dielectric Response: A Theoretical Study. *Nanoscale Res. Lett.* **2010**, *5*, 714–719. [CrossRef]
14. Forte, G.; La Magna, A.; Deretzis, I.; Pucci, R. Ab Initio Prediction of Boron Compounds Arising from Borozene: Structural and Electronic Properties. *Nanoscale Res. Lett.* **2010**, *5*, 158–163. [CrossRef] [PubMed]
15. Bai, H.; Li, S.D. Hydrogenation of $B_{12}^{0/-}$: A Planar-to-Icosahedral Structural Transition in $B_{12}Hn^{0/-}$ (n = 1–6) Boron Hydride Clusters. *J. Clust. Sci.* **2011**, *22*, 525–535. [CrossRef]
16. Ohishi, Y.; Kimura, K.; Yamaguchi, M.; Uchida, N.; Kanayama, T. Hydrogen Detachment from $B_{12}H_n^+$ Clusters by Kinetic Energy. *Trans. Mater. Res. Soc. Jpn.* **2010**, *35*, 533–536. [CrossRef]
17. Ohishi, Y.; Kimura, K.; Yamaguchi, M.; Uchida, N.; Kanayama, T. Synthesis and Formation Mechanism of Hydrogenated Boron Clusters $B_{12}H_n$ with Controlled Hydrogen Content. *J. Chem. Phys.* **2010**, *133*, 074305. [CrossRef] [PubMed]
18. Gonzalez Szwacki, N.; Tymczak, C.J. $B_{12}H$ n and $B_{12}F$ N: Planar vs. Icosahedral Structures. *Nanoscale Res. Lett.* **2012**, *7*, 236. [CrossRef]
19. Zhai, H.J.; Wang, L.S.; Alexandrova, A.N.; Boldyrev, A.I.; Zakrzewski, V.G. Photoelectron Spectroscopy and Ab Initio Study of B_3^- and B_4^- Anions and Their Neutrals. *J. Phys. Chem. A* **2003**, *107*, 9319–9328. [CrossRef]
20. Alexandrova, A.N.; Boldyrev, A.I.; Zhai, H.J.; Wang, L.S.; Steiner, E.; Fowler, P.W. Structure and Bonding in $B6^-$ and B_6: Planarity and Antiaromaticity. *J. Phys. Chem. A* **2003**, *107*, 1359–1369. [CrossRef]
21. Alexandrova, A.N.; Boldyrev, A.I.; Zhai, H.J.; Wang, L.S. Electronic Structure, Isomerism, and Chemical Bonding in B_7^- and B_7. *J. Phys. Chem. A* **2004**, *108*, 3509–3517. [CrossRef]
22. Pan, L.L.; Li, J.; Wang, L.S. Low-Lying Isomers of the B_9^- Boron Cluster: The Planar Molecular Wheel versus Three-Dimensional Structures. *J. Chem. Phys.* **2008**, *129*, 024302. [CrossRef] [PubMed]
23. Martínez-Guajardo, G.; Sergeeva, A.P.; Boldyrev, A.I.; Heine, T.; Ugalde, J.M.; Merino, G. Unravelling Phenomenon of Internal Rotation in B_{13}^+ through Chemical Bonding Analysis. *Chem. Comm.* **2011**, *47*, 6242–6244. [CrossRef] [PubMed]

24. Sergeeva, A.P.; Zubarev, D.Y.; Zhai, H.J.; Boldyrev, A.I.; Wang, L.S. A Photoelectron Spectroscopic and Theoretical Study of B_{16} and B_{16}^{2-}: An All-Boron Naphthalene. *J. Am. Chem. Soc.* **2008**, *130*, 7244–7246. [CrossRef] [PubMed]
25. Sergeeva, A.P.; Averkiev, B.B.; Zhai, H.J.; Boldyrev, A.I.; Wang, L.S. All-Boron Analogues of Aromatic Hydrocarbons: B_{17}^- and B_{18}^-. *J. Chem. Phys.* **2011**, *134*, 224304. [CrossRef] [PubMed]
26. Huang, W.; Sergeeva, A.P.; Zhai, H.J.; Averkiev, B.B.; Wang, L.S.; Boldyrev, A.I. A Concentric Planar Doubly π-Aromatic B_{19} Cluster. *Nat. Chem.* **2010**, *2*, 202–206. [CrossRef]
27. Kiran, B.; Bulusu, S.; Zhai, H.J.; Yoo, S.; Zeng, X.C.; Wang, L.S. Planar-to-Tubular Structural Transition in Boron Clusters: B_{20} as the Embryo of Single-Walled Boron Nanotubes. *Proc. Natl. Acad. Sci. USA* **2005**, *102*, 961–964. [CrossRef]
28. Piazza, Z.A.; Li, W.L.; Romanescu, C.; Sergeeva, A.P.; Wang, L.S.; Boldyrev, A.I. A Photoelectron Spectroscopy and Ab Initio Study of B_{21}^-: Negatively Charged Boron Clusters Continue to Be Planar at 21. *J. Chem. Phys.* **2012**, *136*, 104310. [CrossRef]
29. Sergeeva, A.P.; Piazza, Z.A.; Romanescu, C.; Li, W.L.; Boldyrev, A.I.; Wang, L.S. B_{22}^- and B_{23}^-: All-Boron Analogues of Anthracene and Phenanthrene. *J. Am. Chem. Soc.* **2012**, *134*, 18065–18073. [CrossRef]
30. Popov, I.A.; Piazza, Z.A.; Li, W.L.; Wang, L.S.; Boldyrev, A.I. A Combined Photoelectron Spectroscopy and Ab Initio Study of the Quasi-Planar B_{24}^- Cluster. *J. Chem. Phys.* **2013**, *139*, 144307. [CrossRef]
31. Piazza, Z.A.; Popov, I.A.; Li, W.L.; Pal, R.; Cheng Zeng, X.; Boldyrev, A.I.; Wang, L.S. A Photoelectron Spectroscopy and Ab Initio Study of the Structures and Chemical Bonding of the B_{25}^- Cluster. *J. Chem. Phys.* **2014**, *141*, 034303. [CrossRef] [PubMed]
32. Luo, X.M.; Jian, T.; Cheng, L.J.; Li, W.L.; Chen, Q.; Li, R.; Zhai, H.J.; Li, S.D.; Boldyrev, A.I.; Li, J.; et al. B_{26}^-: The Smallest Planar Boron Cluster with a Hexagonal Vacancy and a Complicated Potential Landscape. *Chem. Phys. Lett.* **2017**, *683*, 336–341. [CrossRef]
33. Li, W.L.; Pal, R.; Piazza, Z.A.; Zeng, X.C.; Wang, L.S. B_{27}^-: Appearance of the Smallest Planar Boron Cluster Containing a Hexagonal Vacancy. *J. Chem. Phys.* **2015**, *142*, 204305. [CrossRef] [PubMed]
34. Li, H.R.; Jian, T.; Li, W.L.; Miao, C.Q.; Wang, Y.J.; Chen, Q.; Luo, X.M.; Wang, K.; Zhai, H.J.; Li, S.D.; et al. Competition between Quasi-Planar and Cage-like Structures in the B_{29}^- Cluster: Photoelectron Spectroscopy and: Ab Initio Calculations. *Phys. Chem. Chem. Phys.* **2016**, *18*, 29147–29155. [CrossRef]
35. Wang, Y.J.; Zhao, Y.F.; Li, W.L.; Jian, T.; Chen, Q.; You, X.R.; Ou, T.; Zhao, X.Y.; Zhai, H.J.; Li, S.D.; et al. Observation and Characterization of the Smallest Borospherene, B_{28}^- and B_{28}. *J. Chem. Phys.* **2016**, *144*, 064307. [CrossRef] [PubMed]
36. Li, W.L.; Zhao, Y.F.; Hu, H.S.; Li, J.; Wang, L.S. $[B_{30}]^-$: A Quasiplanar Chiral Boron Cluster. *Angew. Chem. Int. Ed.* **2014**, *53*, 5540–5545. [CrossRef]
37. Chen, Q.; Li, W.L.; Zhao, X.Y.; Li, H.R.; Feng, L.Y.; Zhai, H.J.; Li, S.D.; Wang, L.S. B_{33}^- and B_{34}^-: Aromatic Planar Boron Clusters with a Hexagonal Vacancy. *Eur. J. Inorg. Chem.* **2017**, *2017*, 4546–4551. [CrossRef]
38. Li, W.L.; Chen, Q.; Tian, W.J.; Bai, H.; Zhao, Y.F.; Hu, H.S.; Li, J.; Zhai, H.J.; Li, S.D.; Wang, L.S. The B_{35} Cluster with a Double-Hexagonal Vacancy: A New and More Flexible Structural Motif for Borophene. *J. Am. Chem. Soc.* **2014**, *136*, 12257–12260. [CrossRef]
39. Piazza, Z.A.; Hu, H.S.; Li, W.L.; Zhao, Y.F.; Li, J.; Wang, L.S. Planar Hexagonal B_{36} as a Potential Basis for Extended Single-Atom Layer Boron Sheets. *Nat. Commun.* **2014**, *5*, 3113. [CrossRef]
40. Chen, Q.; Tian, W.J.; Feng, L.Y.; Lu, H.G.; Mu, Y.W.; Zhai, H.J.; Li, S.D.; Wang, L.S. Planar B_{38}^- and B_{37}^- Clusters with a Double-Hexagonal Vacancy: Molecular Motifs for Borophenes. *Nanoscale* **2017**, *9*, 4550–4557. [CrossRef]
41. Oger, E.; Crawford, N.R.M.; Kelting, R.; Weis, P.; Kappes, M.M.; Ahlrichs, R. Boron Cluster Cations: Transition from Planar to Cylindrical Structures. *Angew. Chem. Int. Ed.* **2007**, *46*, 8503–8506. [CrossRef] [PubMed]
42. Tai, T.B.; Tam, N.M.; Nguyen, M.T. The Boron Conundrum: The Case of Cationic Clusters B_n^+ with n = 2–20. *Theor Chem Acc* **2012**, *131*, 1241. [CrossRef]
43. Dong, X.; Jalife, S.; Vásquez-Espinal, A.; Ravell, E.; Pan, S.; Cabellos, J.L.; Liang, W.Y.; Cui, Z.H.; Merino, G. Li_2B_{12} and Li_3B_{12}: Prediction of the Smallest Tubular and Cage-like Boron Structures. *Angew. Chem. Int. Ed.* **2018**, *57*, 4627–4631. [CrossRef] [PubMed]
44. Hernández-Juárez, G.; Ravell, E.; Arcudia, J.; Zarate, X.; Cui, Z.; Merino, G.; Barroso, J. Structural Effects of Alkali-Metals on the B_{12} Skeleton. *Phys. Chem. Chem. Phys.* **2020**, *22*, 17344–17350. [CrossRef] [PubMed]
45. Contreras, M.; Osorio, E.; Ferraro, F.; Puga, G.; Donald, K.J.; Harrison, J.G.; Merino, G.; Tiznado, W. Isomerization Energy Decomposition Analysis for Highly Ionic Systems: Case Study of Starlike $E_5Li_7^+$ Clusters. *Chem. Eur. J.* **2013**, *19*, 2305–2310. [CrossRef]
46. Barroso, J.; Pan, S.; Merino, G. Structural Transformations in Boron Clusters Induced by Metal Doping. *Chem. Soc. Rev.* **2022**, *51*, 1098–1123. [CrossRef]
47. Solar-Encinas, J.; Leyva-Parra, L.; Yáñez, O.; Inostroza, D.; Barrios-Llacuachaqui, J.R.; Vásquez-Espinal, A.; Orellana, W.; Tiznado, W. Bowl-Shaped CuB_{12}^- Cluster. A Viable Global Minimum with Twofold Aromaticity. *ChemPhysChem* **2022**, *23*, e202200366. [CrossRef]
48. Bai, H.; Zhai, H.-J.; Li, S.-D.; Wang, L.-S. Photoelectron Spectroscopy of Aromatic Compound Clusters of the B_{12} All-Boron Benzene: $B_{12}Au^-$ and $B_{12}(BO)^-$. *Phys. Chem. Chem. Phys.* **2013**, *15*, 9646–9653. [CrossRef]
49. Liu, L.; Moreno, D.; Osorio, E.; Castro, A.C.; Pan, S.; Chattaraj, P.K.; Heine, T.; Merino, G. Structure and Bonding of IrB_{12}^-: Converting a Rigid Boron B_{12} Platelet to a Wankel Motor. *RSC Adv.* **2016**, *6*, 27177–27182. [CrossRef]
50. Shao, X.; Qu, X.; Liu, S.; Yang, L.; Yang, J.; Liu, X.; Zhong, X.; Sun, S.; Vaitheeswaran, G.; Lv, J. Structure Evolution of Chromium-Doped Boron Clusters: Toward the Formation of Endohedral Boron Cages. *RSC Adv.* **2019**, *9*, 2870–2876. [CrossRef]

51. Li, S.X.; Zhang, Z.P.; Long, Z.W.; Chen, D.L. Structures, Electronic, and Spectral Properties of Doped Boron Clusters $MB_{12}^{0/-}$ (M = Li, Na, and K). *ACS Omega* **2020**, *5*, 20525–20534. [CrossRef] [PubMed]
52. Popov, I.A.; Li, W.L.; Piazza, Z.A.; Boldyrev, A.I.; Wang, L.S. Complexes between Planar Boron Clusters and Transition Metals: A Photoelectron Spectroscopy and Ab Initio Study of CoB_{12}^- and RhB_{12}^-. *J. Phys. Chem. A* **2014**, *118*, 8098–8105. [CrossRef] [PubMed]
53. Xiang, Z.; Luo, Z.; Bi, J.; Jin, S.; Zhang, Z.; Lu, C. Structural Evolution and Relative Stability of Vanadium-Doped Boron Clusters. *J. Phys. Condens. Matter* **2022**, *34*, 445302. [CrossRef]
54. le Chen, B.; Sun, W.G.; Kuang, X.Y.; Lu, C.; Xia, X.X.; Shi, H.X.; Maroulis, G. Structural Stability and Evolution of Medium-Sized Tantalum-Doped Boron Clusters: A Half-Sandwich-Structured TaB_{12}^- Cluster. *Inorg. Chem.* **2018**, *57*, 343–350. [CrossRef] [PubMed]
55. Sun, W.; Xia, X.; Lu, C.; Kuang, X.; Hermann, A. Probing the Structural and Electronic Properties of Zirconium Doped Boron Clusters: Zr Distorted B12 Ligand Framework. *Phys. Chem. Chem. Phys.* **2018**, *20*, 23740–23746. [CrossRef] [PubMed]
56. Jin, S.; Chen, B.; Kuang, X.; Lu, C.; Sun, W.; Xia, X.; Gutsev, G.L. Structural and Electronic Properties of Medium-Sized Aluminum-Doped Boron Clusters AlB_n and Their Anions. *J. Phys. Chem. C* **2019**, *123*, 6276–6283. [CrossRef]
57. Yañez, O.; Inostroza, D.; Usuga-Acevedo, B.; Vásquez-Espinal, A.; Pino-Rios, R.; Tabilo-Sepulveda, M.; Garza, J.; Barroso, J.; Merino, G.; Tiznado, W. Evaluation of Restricted Probabilistic Cellular Automata on the Exploration of the Potential Energy Surface of $Be_6B_{11}^-$. *Theor. Chem. Acc.* **2020**, *139*, 41. [CrossRef]
58. Thimmakondu, V.S.; Sinjari, A.; Inostroza, D.; Vairaprakash, P.; Thirumoorthy, K.; Roy, S.; Anoop, A.; Tiznado, W. Why an Integrated Approach between Search Algorithms and Chemical Intuition Is Necessary? *Phys. Chem. Chem. Phys.* **2022**, *24*, 11680–11686. [CrossRef]
59. Oña, O.B.; Alcoba, D.R.; Torre, A.; Lain, L.; Torres-Vega, J.J.; Tiznado, W. Orbital Localization Criterion as a Complementary Tool in the Bonding Analysis by Means of Electron Localization Function: Study of the $Sin(BH)_5$ -N_2^- (n = 0–5) Clusters. *J. Phys. Chem. A* **2013**, *117*, 12953–12958. [CrossRef]
60. Oña, O.B.; Torres-Vega, J.J.; Torre, A.; Lain, L.; Alcoba, D.R.; Vásquez-Espinal, A.; Tiznado, W. Chemical Bonding Analysis in Boron Clusters by Means of Localized Orbitals According to the Electron Localization Function Topology. *Theor. Chem. Acc.* **2015**, *134*, 28. [CrossRef]
61. Zhai, H.-J.; Kiran, B.; Li, J.; Wang, L.-S. Hydrocarbon Analogues of Boron Clusters—Planarity, Aromaticity and Antiaromaticity. *Nat. Mater.* **2003**, *2*, 827–833. [CrossRef] [PubMed]
62. Yañez, O.; Báez-Grez, R.; Inostroza, D.; Rabanal-León, W.A.; Pino-Rios, R.; Garza, J.; Tiznado, W. AUTOMATON: A Program That Combines a Probabilistic Cellular Automata and a Genetic Algorithm for Global Minimum Search of Clusters and Molecules. *J. Chem. Theory Comput.* **2019**, *15*, 1463–1475. [CrossRef] [PubMed]
63. Adamo, C.; Barone, V. Toward Reliable Density Functional Methods without Adjustable Parameters: The PBE0 Model. *J. Chem. Phys.* **1999**, *110*, 6158–6170. [CrossRef]
64. Fuentealba, P.; Von Szentpaly, L.; Preuss, H.; Stoll, H. Pseudopotential Calculations for Alkaline-Earth Atoms. *J. Phys. B At. Mol.Opt.* **1985**, *18*, 1287–1296. [CrossRef]
65. Grimme, S.; Antony, J.; Ehrlich, S.; Krieg, H. A Consistent and Accurate Ab Initio Parametrization of Density Functional Dispersion Correction (DFT-D) for the 94 Elements H-Pu. *J. Chem. Phys.* **2010**, *132*, 154104. [CrossRef] [PubMed]
66. Weigend, F.; Ahlrichs, R. Balanced Basis Sets of Split Valence, Triple Zeta Valence and Quadruple Zeta Valence Quality for H to Rn: Design and Assessment of Accuracy. *Phys. Chem. Chem. Phys.* **2005**, *7*, 3297. [CrossRef] [PubMed]
67. Riplinger, C.; Pinski, P.; Becker, U.; Valeev, E.F.; Neese, F. Sparse Maps—A Systematic Infrastructure for Reduced-Scaling Electronic Structure Methods. II. Linear Scaling Domain Based Pair Natural Orbital Coupled Cluster Theory. *J. Chem. Phys.* **2016**, *144*, 024109. [CrossRef] [PubMed]
68. Neese, F. The ORCA Program System. *Wiley Interdiscip. Rev. Comput. Mol. Sci.* **2012**, *2*, 73–78. [CrossRef]
69. Neese, F. Software Update: The ORCA Program System, Version 4.0. *Wiley Interdiscip. Rev. Comput. Mol. Sci.* **2018**, *8*, 73–78. [CrossRef]
70. Truhlar, D.G. Basis-Set Extrapolation. *Chem. Phys. Lett.* **1998**, *294*, 45–48. [CrossRef]
71. Neese, F.; Hansen, A.; Liakos, D.G. Efficient and Accurate Approximations to the Local Coupled Cluster Singles Doubles Method Using a Truncated Pair Natural Orbital Basis. *J. Chem. Phys.* **2009**, *131*, 064103. [CrossRef] [PubMed]
72. Glendening, E.D.; Badenhoop, J.K.; Reed, A.E.; Carpenter, J.E.; Bohmann, J.A.; Morales, C.M.; Landis, C.R.; Weinhold, F. *Natural Bond Orbital Analysis Program: NBO 6.0*; Theoretical Chemistry Institute, University of Wisconsin: Madison, WI, USA, 2013.
73. Zubarev, D.Y.; Boldyrev, A.I. Developing Paradigms of Chemical Bonding: Adaptive Natural Density Partitioning. *Phys. Chem. Chem. Phys.* **2008**, *10*, 5207–5217. [CrossRef] [PubMed]
74. Zubarev, D.Y.; Boldyrev, A.I. Revealing Intuitively Assessable Chemical Bonding Patterns in Organic Aromatic Molecules via Adaptive Natural Density Partitioning. *J. Org. Chem.* **2008**, *73*, 9251–9258. [CrossRef]
75. Lu, T.; Chen, F. Multiwfn: A Multifunctional Wavefunction Analyzer. *J. Comput. Chem.* **2012**, *33*, 580–592. [CrossRef]
76. Grimme, S.; Ehrlich, S.; Goerigk, L. Effect of the Damping Function in Dispersion Corrected Density Functional Theory. *J. Comput. Chem.* **2011**, *32*, 1456–1465. [CrossRef]
77. Van Lenthe, E.; Baerends, E.J.; Snijders, J.G. Relativistic Total Energy Using Regular Approximations. *J. Chem. Phys.* **1994**, *101*, 9783–9792. [CrossRef]

78. Van Lenthe, E.; Baerends, E.J. Optimized Slater-Type Basis Sets for the Elements 1–118. *J. Comput. Chem.* **2003**, *24*, 1142–1156. [CrossRef] [PubMed]
79. Baerends, E.J.; Ziegler, T.; Atkins, A.J.; Autschbach, J.; Baseggio, O.; Bashford, D.; Bérces, A.; Bickelhaupt, F.M.; Bo, C.; Boerritger, P.M.; et al. *ADF2012. 01; SCM, Theoretical Chemistry*; Vrije Universiteit: Armsterdam, The Netherland, 2012.
80. Jusélius, J.; Sundholm, D.; Gauss, J. Calculation of Current Densities Using Gauge-Including Atomic Orbitals. *J. Chem. Phys.* **2004**, *121*, 3952–3963. [CrossRef] [PubMed]
81. Fliegl, H.; Taubert, S.; Lehtonen, O.; Sundholm, D. The Gauge Including Magnetically Induced Current Method. *J. Chem. Phys.* **2011**, *13*, 20500–20518. [CrossRef]
82. Wolinski, K.; Hinton, J.F.; Pulay, P. Efficient Implementation of the Gauge-Independent Atomic Orbital Method for NMR Chemical Shift Calculations. *J. Am. Chem. Soc.* **1990**, *112*, 8251–8260. [CrossRef]
83. Ayachit, U.; Geveci, B.; Moreland, K.; Patchett, J.; Ahrens, J. The ParaView visualization application. In *High Performance Visualization—Enabling Extreme-Scale Scientific Insight*; Bethel, E.W., Childs, H., Hansen, C., Eds.; Taylor & Francis: Abingdon, UK, 2012; pp. 383–400.
84. Ahrens, J.; Geveci, B.; Law, C. Paraview: An End-User Tool for Large Data Visualization. In *The Visualization Handbook*; Elsevier Academic Press Cambridge: Cambridge, MA, USA, 2005; Volume 717.
85. Abramowitz, M. *Handbook of Mathematical Functions, with Formulas, Graphs, and Mathematical Tables*; Dover Publications, Inc.: New York, NY, USA, 1974.
86. Keith, T.A. *AIMAll*, Version 19.10. 12; TK Gristmill Software: Overland Park, KS, USA, 2019.
87. Sundholm, D.; Berger, R.J.F.; Fliegl, H. Analysis of the Magnetically Induced Current Density of Molecules Consisting of Annelated Aromatic and Antiaromatic Hydrocarbon Rings. *Phys. Chem. Chem. Phys.* **2016**, *18*, 15934–15942. [CrossRef] [PubMed]
88. Inostroza, D.; García, V.; Yañez, O.; Torres-Vega, J.J.; Vásquez-Espinal, A.; Pino-Rios, R.; Báez-Grez, R.; Tiznado, W. On the NICS Limitations to Predict Local and Global Current Pathways in Polycyclic Systems. *New J. Chem.* **2021**, *45*, 8345–8351. [CrossRef]